

AstroSat UV Deep Field IV. An Extended UV disk around a massive spiral galaxy at $z=0.67$

Pushpak Pandey¹,^{*} Kanak Saha¹, Sanchayeeta Borthakur²

¹Inter-University Centre for Astronomy and Astrophysics, Ganeshkhind, Post Bag 4, Pune 411007, India

²School of Earth and Space Exploration, Arizona State University, 781 E Terrace Mall, Tempe, AZ 85287-1404, USA

Accepted XXX. Received YYY; in original form ZZZ

ABSTRACT

Extended ultraviolet (XUV) emission in nearby disk galaxies supports the inside-out growth scenario through low-efficiency star formation in their outer regions. However, such detections have largely been limited to the local Universe ($z \sim 0$) due to the need for deep, high-resolution UV imaging. We report the detection of a clumpy XUV disk in a massive, isolated spiral galaxy ($\log(M_*/M_\odot) \approx 11.04$) at $z = 0.67$, observed with AstroSat/UVIT. The intrinsic rest frame FUV surface brightness profile, corrected for the instrument PSF, shows a more extended disk than its optical and IR counterparts. The XUV disk reaches nearly twice the optical radius and includes a large UV-bright low surface brightness (LSB) region ($S_{LSB}/S_{K80} \approx 9.3$, $\mu_{FUV} - \mu_K \approx 1$), consistent with the Type II XUV definition. Additionally, the detection of UV clumps without optical counterparts supports a Type I classification, suggesting gravitational instabilities and recent star formation. These features point to recent cold gas accretion onto the outer disk. From the asymmetric light profile, we estimate a gas accretion rate of $\sim 11 M_\odot \text{ yr}^{-1}$, providing evidence of active disk growth at intermediate redshift.

Key words: galaxies: star formation – Galaxy: disc – Galaxy: evolution – galaxies: spiral

1 INTRODUCTION

The process of galaxy growth and evolution can be directly attributed to the process of star formation, as it can be triggered by various phenomena such as disk instabilities, mergers, gas accretion (Dekel et al. 2009a; Hopkins et al. 2008; Kennicutt & Evans 2012; Somerville & Davé 2015), etc. Hence, star formation can act as a reliable tracer for such events. One such mechanism that may cause recent star formation in the outer disk region is the infall of cold gas from the intergalactic medium (IGM), which can form star-forming clumps around the disk and result in extended ultraviolet (XUV) emission beyond the conventional star formation threshold. This phenomenon was first observed in galaxies such as NGC 4625 (Gil de Paz et al. 2005) and M83 (Thilker et al. 2005).

Galaxies with such extended UV emission beyond the star formation threshold surface brightness ($\mu_{FUV} = 27.25 \text{ mag arcsec}^{-2}$ or $\Sigma_{SFR} = 3 \times 10^{-4} M_\odot \text{ yr}^{-1} \text{ kpc}^{-2}$) are termed XUV disks. According to Thilker et al. (2007) (T07), such systems are classified as Type I XUV disks if they show discrete UV-bright clumps in the outer disk, and Type II if the star formation is more diffuse, covering a low surface brightness (LSB) zone beyond the K_{80} radius, the radius enclosing 80% of the rest-frame K -band light, and within R_{SFR} , the radius where restframe FUV magnitude is equal to the SFR threshold ($\mu_{FUV} = 27.25$). These definitions have since been widely used in follow-up studies (Lemonias et al. 2011; Moffett et al. 2012; Das et al. 2021). Other works have also used the R_{25} radius (Zaritsky & Christlein 2007; Goddard et al. 2010) or break radius in surface

brightness (SB) profiles (Pohlen & Trujillo 2006; Sarkar & Saha 2024) to define the XUV region (Padave et al. 2021).

The extent of XUV emission in such galaxies often extends 2–4 times beyond their optical extents and is directly correlated with the distribution of HI gas, which is known to reach much farther out than the stellar disk (Thilker et al. 2005; Zaritsky & Christlein 2007; Padave et al. 2024). Extended star formation in these outer regions can be driven by several processes, such as gas accretion from the IGM (often inferred from low metallicities; Gil de Paz et al. 2007b; Goddard et al. 2011), tidal interactions (Neff et al. 2005; López-Sánchez et al. 2015), spiral density waves, or even radiative cooling (Dekel & Birnboim 2006). While galactic winds may redistribute gas within the disk, they are generally considered secondary contributors (Thilker et al. 2007).

From the perspective of galaxy evolution, the detection of XUV emission supports the inside-out disk growth paradigm (Thilker et al. 2007; Muñoz-Mateos et al. 2007; Borgohain et al. 2022; Padave et al. 2024) and allows us to trace how galaxies build up their outer disks over time. Moreover, these XUV zones, particularly when forming stars at high sSFR ($\log \text{sSFR} > -9$) and low stellar mass surface densities, can be considered localised starburst regions. Such rapid and concentrated star formation may have consequences on the interstellar medium (ISM). However, given the low stellar densities and the likely absence of sustained supernova (SN) feedback in these outer regions, the ISM properties in the XUV zone may be markedly different from the more evolved ISM of the central disk.

XUV disks are found in ~ 20 – 30% of nearby disk galaxies (Thilker et al. 2007; Gil de Paz et al. 2007a; Lemonias et al. 2011). While the phenomenon is often associated with spiral galaxies, extended UV emission is also observed in some blue early-type systems (Moffett

* E-mail: pushpak@iucaa.in

et al. 2012; Dhiwar et al. 2023), which may be rebuilding their disks. Due to the diversity in morphology, these galaxies span a wide region in the colour–magnitude diagram. The detected number density of XUV disks appears relatively uniform across stellar mass bins, but their relative fraction is higher in the high-mass regime (Lemonias et al. 2011).

However, detecting such XUV features at higher redshifts is observationally challenging due to their low surface brightness and the need for sub-kpc resolution. GALEX-based studies have been largely limited to the nearby Universe ($z \lesssim 0.05$). A rare example of intermediate-redshift XUV detection is provided by Borgohain et al. (2022) (B22), using UVIT data to identify extended UV emission in blue compact dwarfs at $z \sim 0.1$ – 0.24 using PSF-corrected SB profile fitting. In this work, we present the discovery of an XUV disk in a massive spiral galaxy at $z \approx 0.67$, observed via the N242W band of UVIT onboard AstroSat. This is the most distant and most massive star-forming spiral galaxy hosting an XUV disk to date.

In the following sections, we describe our data, and the disk modeling process (similar to B22) used to estimate the UV star formation threshold radius and K_{80} . We further estimate the gas accretion rate from lopsidedness in the stellar disk, and discuss this system’s properties in comparison with literature XUV samples to build a case for its inside-out disk growth

2 DATA

The galaxy AUDFs_N02766 (Saha et al. 2024, also cataloged as GOODS-S 38092; Skelton et al. 2014), shown in Figure 1a, is located at ICRS coordinates RA = 53.1251°, Dec = −27.7299° (J2000), with a redshift of $z = 0.668$, corresponding to a lookback time of approximately 6.12 Gyr. It is a massive, star-forming disk galaxy with prominent spiral arms, clumps, and a significant bulge visible in UV, optical and infrared bands, see Figure 1(a, b, c). In HST imaging, it spans $\sim 9''$ along the semi-major axis - approximately 63 kpc - assuming a flat Λ CDM cosmology with $H_0 = 70$ km/s/Mpc and $\Omega_m = 0.3$ (used throughout this work).

We utilize archival GOODS-South observations from HST/ACS and WFC3 (Windhorst et al. 2011; Illingworth et al. 2016; Whitaker et al. 2019), VLT/ISAAC (Retzlaff et al. 2010), and Spitzer/IRAC (Stefanon et al. 2021), as well as UVIT-AstroSat data (Saha et al. 2024). The galaxy’s redshift is further confirmed through its optical spectrum from VLT/VIMOS (Balestra et al. 2010), classified as Quality ‘A’ with clearly detected features including the Balmer 4000 Å break, [O III] doublet, and Ca II H & K absorption lines (see supplementary material).

3 PHOTOMETRY AND SED FITTING

To enable consistent flux measurements across multiple filters from different telescopes, the HST and ISAAC images are matched to UVIT/N242W PSF using the Photutils (Bradley et al. 2024). Since the F154W band is already closely matched beyond $r > 2''$, it requires no further adjustment (Saha et al. 2024). Due to the broad PSF of IRAC-2, 3, and 4 channels, we use aperture-corrected fluxes from the original images to avoid contamination from neighbouring sources. A common $4.58''$ radius circular aperture was applied across all PSF-convolved images and their associated weight maps, centered on the bulge of the galaxy, to estimate fluxes and their uncertainties. Background and Poisson errors are calculated for the UVIT bands

following Pandey & Saha (2025). Aperture corrected fluxes (converted to mJy and corrected for foreground extinction using Schlafly & Finkbeiner 2011) are then used to construct the broadband SED (1300Å – 9.5 μ m) for the galaxy. We fit the SED using CIGALE (Boquien 2020) employing double exponential SFH, BC03 stellar population models, and Milky Way dust attenuation law. The best-fitting SED (reduced $\chi^2 = 1.2$, Figure 2) gives a total stellar mass of $1.08 \times 10^{11} M_\odot$, a young stellar mass of $2.54 \times 10^9 M_\odot$ (100 Myr), a star formation rate of $28.1 \pm 1.4 M_\odot \text{ yr}^{-1}$, and $E(B - V) = 0.132$. For more details on photometry and SED modelling, see the supplementary material.

4 MODELLING OF RADIAL DISK PROFILES

In order to extract the radial surface brightness (SB) profile of the galaxy, we first estimate the disk ellipticity (ϵ) and position angle (PA) using the HST/F160W image (Figure 1a). This is done by fitting isophotes with the Ellipse fitting routine, keeping the center fixed at the centroid of the bulge. While spiral arms in the inner region ($R < 3.5''$) influence the isophotal shape, the outer isophotes are relatively stable and yield a mean ellipticity of $\epsilon = 0.2$ and PA of $41.8^\circ \pm 0.8^\circ$. Using these parameters, we construct a set of elliptical annuli centered on the bulge and applied to all the cutout images in the optical/IR filters to extract the radial profiles and corresponding errors. However, the rest-frame FUV SB profile has been extracted from the observed N242W filter image, to which we first mask the foreground/background sources using the Whitaker et al. (2019) segmentation map, convolved with a top-hat kernel of $2 \times$ the N242W PSF FWHM. The resulting SB profile shows a flat core within $\sim 3''$, modeled by a Sérsic function, while the outer disk follows an exponential (see Figure 1d). We employ the same masking procedure to the Spitzer/IRAC-1 ($\sim 3.6\mu\text{m}$) image, to derive the rest-frame K -band profile. Note that for all the HST images, the masks are applied without convolution.

We consider a forward modelling approach to derive the intrinsic SB profile of the galaxy in a given passband. In this process, we first convolve a presumed model (say, exponential or Sersic profile) with a PSF and then fit the convolved profile with observed SB data to extract the best-fit model parameters. We employ the astropy.modeling framework (Astropy Collaboration et al. 2022) to generate two-dimensional exponential disk and Sersic models at the same pixel scale as the observed images. These models are convolved with the respective PSF and sampled using the same elliptical annuli (used to extract observed SB profile) to produce model 1D profiles. We then fit these to the observed galaxy profiles using the least-squares routine from scipy.optimize (Virtanen et al. 2020). A direct approach with 2D modelling using GALFIT (Peng et al. 2010) was tested but due to the SNR of individual pixels being low, we couldn’t reach a reasonable fitting for the XUV region. In most HST and ISAAC images, we find that beyond a radius of $\sim 4.5''$, the profiles show negative flux values. This indicates over-subtraction of the local background and results in a sharp decline in the radial profile near $\sim 4.5''$ (F140W profile in Figure 1d).

These SB profiles were corrected for cosmological surface brightness dimming (Tolman 1930, 1934) due to redshift which comes out at $A_{\text{cosmo}} = -1.67$. And also corrected for internal dust attenuation using the Calzetti et al. (2000) extinction law, assuming a uniform color excess $E(B - V)$ from our best-fit SED, which provides a correction value of $A_{\text{dust}, \text{FUV}} = -1.227$ for rest frame FUV, and $A_{\text{dust}, \text{Ks}} \approx 0$ for rest frame Ks. The foreground dust was also corrected using the Milkyway dustmaps (Schlegel et al. 1998; Schlafly &

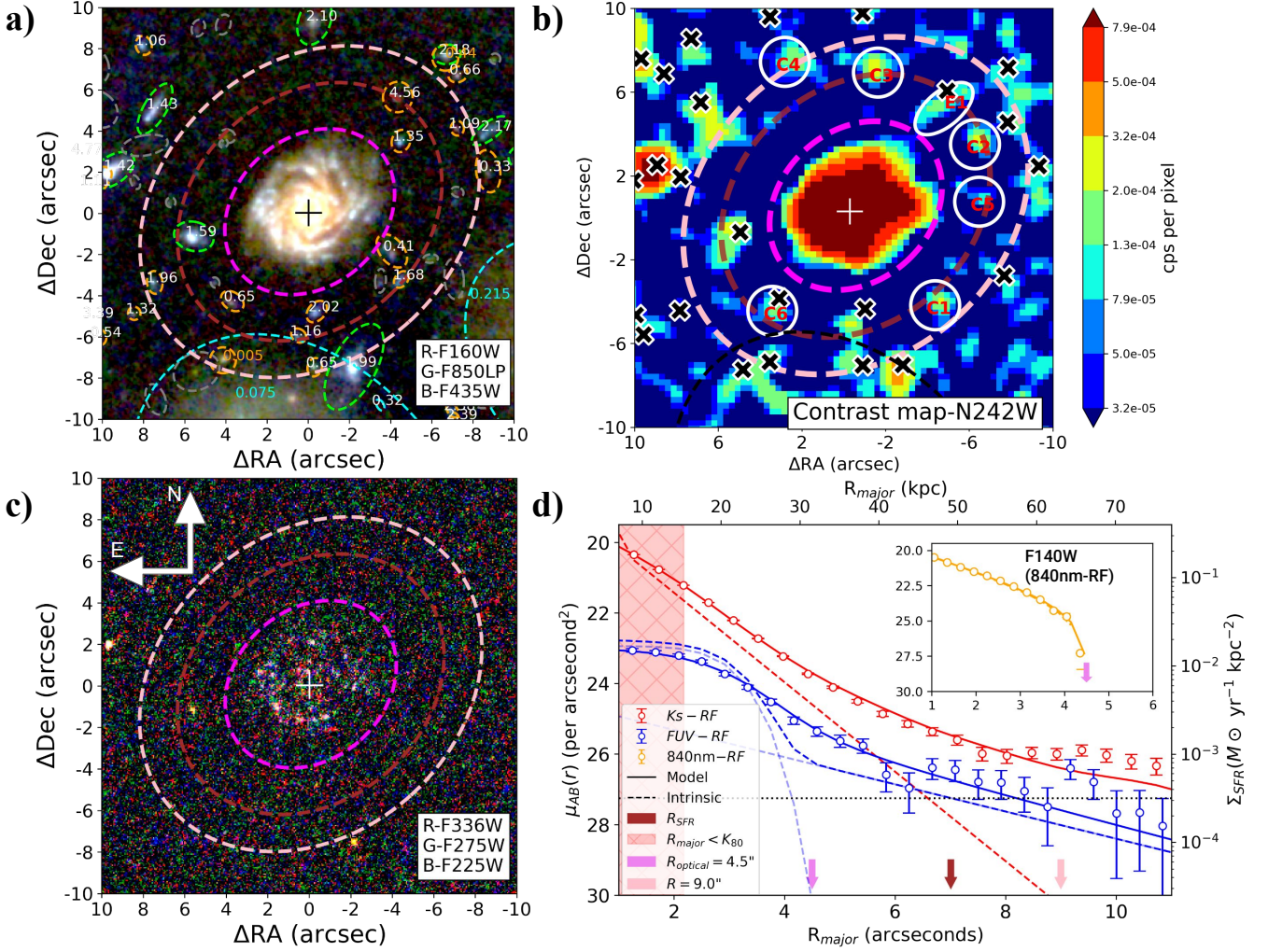


Figure 1. (a) RGB image of ADFs_N02766 using HST bands: F160W (red), F850LP (green), and F435W (blue). Nearby HST detections (HLF catalog) are marked with dashed ellipses; redshift types are colour-coded: cyan (spectroscopic), green (grism), orange (photometric), and gray (unknown). The magenta ellipse denotes the optical edge ($R_{major} \sim 4.5''$); the pink ellipse outlines the XUV disk at $SNR > 3$ ($R_{major} \sim 9''$); the brown ellipse marks the SFR threshold ($\mu_{FUV} = 27.25$). (b) Contrast map of ADFs_N02766 in UVIT-N242W, obtained via an unsharp-masking procedure, showing HST counterparts of UV detections (black crosses), detected clumps (white circles, $r = 1$ PSF FWHM) with red IDs, and an extended feature labelled E1. The bottom foreground galaxy ($z \sim 0.075$), which is particularly bright in UV, has its boundaries marked with a black dashed ellipse. (c) HST-UV RGB image (F336W, F275W, F225W) showing the bulgeless UV disk and resolved clumps within the optical boundary ($R < 4.5''$). (d) Surface brightness profiles in rest frame K_s (IRAC-1), rest frame FUV (UVIT-N242W), and (inset) rest frame 840nm (HST-F140W), corrected for cosmological dimming and extinction. PSF-convolved models (solid), intrinsic models (dashed), and seric+ exponential for N242W (faint dashed) are shown. K_{80} marks 80% light radius of rest frame K_s (IRAC-1) model; R_{SFR} (brown arrow) marks $\mu_{FUV} = 27.25$; magenta arrow shows optical edge at $4.5''$ (31.5 kpc), and pink arrow marks the end of our XUV-detection boundary at $9''$ (63 kpc).

Finkbeiner 2011), which gives a correction factor of $A_{fore} = -0.054$ and 0 for N242 and IRAC-1 respectively. Together, all of these magnitude corrections add up to $\Delta m_{corr, FUV} \approx -3$ for Rest frame FUV, and $\Delta m_{corr, K_s} \approx -1.67$ for restframe K_s magnitudes and Surface brightness (More details on Surface Brightness profile corrections are presented in Appendix F of supplementary material). The SB profiles and intrinsic disk models of dust corrected rest-frame FUV (N242W), rest-frame K_s (IRAC-1) and rest frame NIR (F140W) are presented in Figure 1d. The intrinsic scale lengths derived from best-fit model in various bands are summarised in Table 1. There seems to be a mild trend of increasing disk scale length at bluer filters.

5 THE CLUMPY XUV DISK

Here, we follow the criteria outlined by T07, to characterise the extended ultraviolet (XUV) disk of ADFs_N02766. First, the intrinsic radial SB profiles of ADFs_N02766 in the rest-frame FUV and K_s bands are being compared. A surface density threshold of $3 \times 10^{-4} M_{\odot} \text{ yr}^{-1} \text{ kpc}^{-2}$ — equivalent to $\mu_{FUV} = 27.25 \text{ mag arcsec}^{-2}$ — is adopted to mark the SFR limit in the rest frame FUV profile. The corresponding R_{SFR} is indicated by the brown marker in Figure 1d.

The radius encompassing 80% of the total intrinsic restframe K_s band flux is $K_{80} = 2.18''$, while the rest frame FUV disk extends out to $R_{SFR} = 7.0''$, where the corrected rest-frame FUV surface

Filter	Restframe λ	Disk R_s (Kpc)	mag ₀	SNR	Contamination
Global Properties					
Irac-1	2200 nm	6.3 ± 0.08	18.80 ± 0.001	–	–
Isaac K_s	1320 nm	6.1 ± 0.14	18.98 ± 0.02	–	–
HST-F160W	960 nm	6.5 ± 0.14	19.09 ± 0.002	–	–
HST-F140W	840 nm	7.1 ± 0.09	19.34 ± 0.006	–	–
HST-F775W	464 nm	7.4 ± 0.5	20.12 ± 0.004	–	–
HST-F660W	363 nm	6.5 ± 0.5	20.98 ± 0.005	–	–
N242W	145 nm	20.0 ± 2.9 (XUV)	22.19 ± 0.02	–	–
UV clump properties					
N242W (C1)	145 nm	–	27.16 ± 0.25	4.3	No
N242W (C2)	145 nm	–	27.32 ± 0.27	3.76	No
N242W (C3)	145 nm	–	27.19 ± 0.26	4.17	No
N242W (C4)	145 nm	–	27.53 ± 0.35	3.16	No
N242W (C5)	145 nm	–	27.49 ± 0.34	3.27	No
N242W (C6)	145 nm	–	27.07 ± 0.24	4.6	phot-z ~ 0.65 *
N242W (E1)	145 nm	–	27.00 ± 0.20	4.84	phot-z $\sim 4.56^\dagger$

Table 1. Global Properties of AUDFs_N02766, along with detected UV clump properties. Observed magnitudes in the filters (mag₀) and Disk scalelengths (R_s) are shown for the galaxy in separate filters. For clumps, shown in Figure 1b, we show mag₀ (in PSF FWHM sized aperture) and signal-to-noise ratios (SNR). Possible contamination by nearby sources from the HLF catalog (within a 1.2'' aperture radius) is noted. Notes: * The phot-z estimate is similar to AUDFs_N02766. † Phot-z estimate of 4.56 places the N242W band in the Lyman continuum, where the transmission probability is very low (Inoue et al. 2006; Saha et al. 2020).

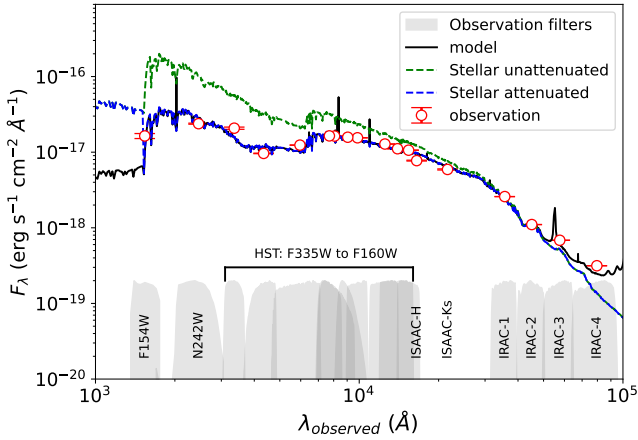


Figure 2. The best-fit SED model (black) is shown alongside the observed fluxes (red points). The attenuated and unattenuated stellar continua are shown as blue and green dashed lines, respectively. The reduced χ^2 for the fit is 1.2. The transmission curves (scaled) of the filters used in the fitting are overlaid as grey shaded regions.

brightness reaches the SFR threshold (see Figure 1d). The low surface brightness (LSB) zone, defined between K_{80} and R_{SFR} , exhibits a color difference of $\mu_{FUV} - \mu_{K_s} = 0.99$, and spans an area ~ 9.34 times larger than the inner K_{80} region. These criteria are consistent with a Type II XUV disk as per T07, which required the area of LSB zone (S_{LSB}) to be at least 7 times the K_{80} region (S_{K80}), and the color $\mu_{FUV} - \mu_{K_s} < 4$.

The intrinsic rest-frame FUV SB profile shows a noticeable transition from the bright inner disk to the fainter extended component at $\sim 4-4.5''$, which coincides with the outer optical edge observed in most HST bands. Beyond this radius, the 1D profiles in the HST optical images drop below zero, likely due to background over subtraction. This suggests that the faint, extended disk is no longer visible in the optical bands but remains detectable in the UV.

In the HST UV bands (Fig. 1c), the galaxy shows a faint disk with a ring-like structure, most prominent towards the south-east

and weaker towards the north-west, formed by UV clumps along the spiral arms. A model comprising only the HST-UV disk and this ring-like structure, convolved with the N242W PSF, does not reproduce the total UV emission observed in the XUV region in the N242W band. The integrated magnitude difference between the PSF-convolved HST-UV model and the N242W profile in the XUV region is $\Delta m_{XUV} \approx -0.6 \pm 0.07$, corresponding to an excess of 41 ± 4 per cent in N242W. This excess emission indicates the presence of an extended XUV disk (see Appendix E).

To classify the XUV disk of AUDFs_N02766 as Type I, we run SExtractor with high deblending on the N242W image and identify several faint, clumpy UV structures (with $SNR > 3$) beyond R_{SFR} . To validate and visually cross check these clumps, we create a contrast map via an unsharp masking procedure and scaling the image by $2\times$ length using spline interpolation. During this process, we remove the UV clumps with optical counterparts within a PSF FWHM radius ($1.2''$). Many of these clumpy structures are identified at an $r > R_{SFR}$ which is consistent with the Type I XUV disk definition (Thilker et al. 2007) (Figure 1b). The photometric details of each detected clump is provided in Table 1. A similar analysis with the archival HST/F225W and F275W data does not reveal these UV clumps, likely due to insufficient depth. We mark the XUV disk as the region beyond the $4.5''$ radius, which extends to $\sim 9''$ in far-UV. Additional details of clump detections and clump properties are discussed in the supplementary material.

From the intrinsic surface brightness model of the rest-frame FUV, we calculate the integrated UV-based star formation rate (SFR) in the XUV region ($4.5'' < R < 9''$) to be approximately $2.8 M_{\odot} \text{ yr}^{-1}$ (Kennicutt 1998). Assuming a constant SFR over the past 100 Myr, this implies a young stellar mass of $\sim 2.8 \times 10^8 M_{\odot}$ formed in this region, which is $\sim 10\%$ of the total young stellar population obtained via SED modelling in section 3.

6 LOPSIDEDNESS AND GAS ACCRETION RATE

Visual inspection of the HST images of AUDFs_N02766 reveals a lopsided asymmetry in the light distribution along the galaxy's semi-major axis, particularly toward the north-west, relative to the central

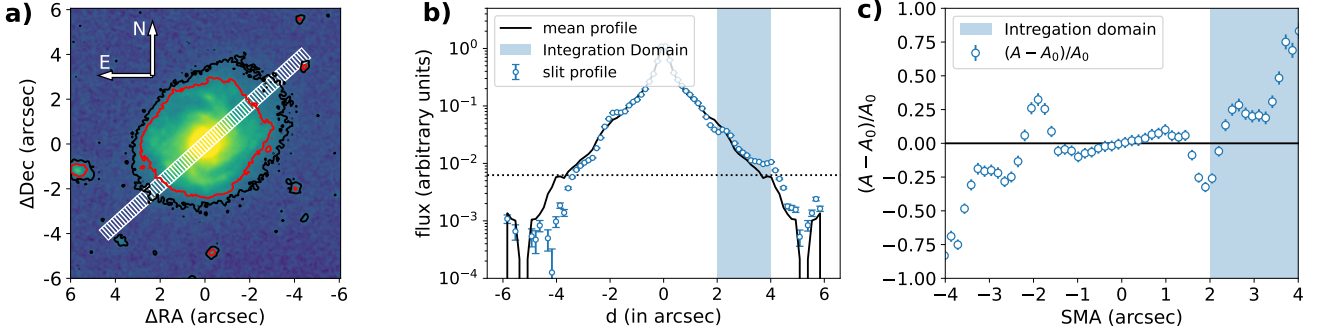


Figure 3. (a) False-color image of stacked HST bands (F125W, F140W, F160W) with 1σ (black) and 3σ (red) isophotal contours overlaid. A white slit is placed along the direction of observed lopsidedness. (b) Light profile of AUDFs_N02766 along the slit (blue markers) compared to the mean profile (A_0 , black). The black horizontal dotted line represents the 1σ level shown in (a). (c) Radial variation of A_1/A_0 . The mean $\langle A_1/A_0 \rangle$ is computed over the radial range highlighted in the blue region.

bulge (Figure 3). This asymmetry is subtle in the N242W image. Additionally, the N242W data show an elongated clumpy structure in the same direction (marked as E1 in Figure 1b). The prevalence of these asymmetric features help us understand gas inflow via angular momentum transport (Saha & Jog 2014). While quantifying these asymmetries provides a useful proxy to estimate the galaxy’s recent gas accretion activity (Zaritsky & Rix 1997; Jog & Combes 2009). In order to estimate asymmetries in the galactic disk, we perform a Fourier decomposition of the light distribution:

$$A(r, \phi) = A_0(r) + \sum_{m=1}^{\infty} A_m(r) e^{in(\phi - \phi_m)}, \quad (1)$$

where $A(r, \phi)$ is the observed surface brightness, $A_0(r)$ is the azimuthally averaged radial profile, and A_m and ϕ_m are the amplitude and phase of the m -th Fourier component. The $m = 1$ mode quantifies lopsidedness, while higher-order terms ($m \geq 2$) capture finer asymmetries such as spiral arms or clumps (Rix & Zaritsky 1995). To quantify lopsidedness, we follow the method of Rix & Zaritsky (1995); Zaritsky & Rix (1997), estimating A_1 by fitting sinusoidal modes to the 2D light distribution $A(r, \phi)$. The HST/F160W intensity map is binned into a 25×25 grid in polar coordinates spanning $0 < r < 4.5''$, and $0 < \theta < 2\pi$. We compute the mean fractional lopsidedness $\langle A_1/A_0 \rangle$ in the radial range $2'' < r < 4''$, where the A_1 phase angle is nearly flat. We find $\langle A_1/A_0 \rangle = 0.27 \pm 0.007$ in F160W, and 0.21 ± 0.009 in ISAAC- K_s . The phase angle of the A_1 mode is $64.9^\circ \pm 1.7^\circ$ in F160W and $67.6^\circ \pm 4.0^\circ$ in K_s , implying an offset of $\sim 23 - 25^\circ$ from the Position angle of the galaxy.

To independently confirm this measurement, we co-add HST: F125W, F140W, and F160W images (PSF-matched and weighted by inverse variance), and extract a 1D light profile along a custom slit aligned with the galaxy’s position angle (see Figure 3a). With the azimuth fixed, the light profile $A(r)$ can be decomposed as:

$$A(r) \approx A_0(r) + A_1(r) \quad (2)$$

where r runs from $-L/2$ to $L/2$ along the slit, and $A_0(|r|) = \frac{1}{2} [A(-r) + A(r)]$. The lopsided component is computed as $A_1 = A - A_0$, and the relative amplitude A_1/A_0 is measured as a function of r (Figure 3c). Averaging over $2'' < r < 4''$, we find $\langle A_1/A_0 \rangle = 0.260 \pm 0.002$, in agreement with the 2D Fourier result. According to Zaritsky & Rix (1997), a lopsidedness amplitude $\langle A_1/A_0 \rangle \geq 0.2$ is indicative of a galaxy that has accreted $\sim 10\%$ of

its mass within the past 1 Gyr. Assuming low merger activity (as the galaxy resides in a low density environment), for AUDFs_N02766, this corresponds to an average gas accretion rate of $\sim 11 M_\odot \text{ yr}^{-1}$. This rate is enough to replenish the depleting gas reservoirs in the XUV region, as the calculated UV SFR of $2.8 M_\odot \text{ yr}^{-1}$ is less than the gas accretion rate calculated above.

7 DISCUSSION

7.1 Efficiency of UV disk models as a reliable UV SFR tracer

A key limitation in determining the SFR threshold radius from UVIT observations arises from its point-spread function (PSF). The N242W band has a PSF FWHM of $1.2''$, corresponding to a physical scale of ~ 8.4 kpc at $z = 0.67$, in contrast to the ~ 1 kpc resolution of HST/F225W and F275W (Figure 1c). Despite this lower spatial resolution, UVIT achieves a 3σ limiting magnitude of 27.73 mag (within a $1.2''$ aperture), deeper than the ~ 25.9 mag limits of the archival HST UV data (Windhorst et al. 2011) (more in the supplementary material). This makes UVIT more sensitive to diffuse and faint features such as extended UV (XUV) emission and disjoint clumps that remain undetected in HST UV bands.

However, the broader PSF in N242W leads to flux boosting in the galaxy’s outer regions, potentially biasing the inferred SFR threshold radius outward. To mitigate this effect, we apply a PSF-corrected disk-fitting algorithm to reconstruct the intrinsic radial surface brightness (SB) profile in the rest-frame FUV.

Our Type II XUV disk classification is based on modelling the rest-frame FUV profiles corrected for dust attenuation from the SED model. If measurements are done without any dust correction, the SFR limit radius reduces to $\sim 4.23''$, decreasing the LSB region to $\sim 3 \times K_{80}$ region, and yielding a color of $\mu_{\text{FUV}} - \mu_{K_s} \sim 2.26$. These values no longer satisfy the criteria for a Type II XUV disk as per Thilker et al. (2007). Thus, without a radial attenuation model, which is not feasible with the current dataset, the Type II classification of AUDFs_N02766 faces uncertainty. Nevertheless, the detection of multiple isolated UV-bright clumps and the faint exponential disk in the outer region (beyond the SFR threshold radius), without optical counterparts, supports the identification of AUDFs_N02766 as a Type I XUV disk.

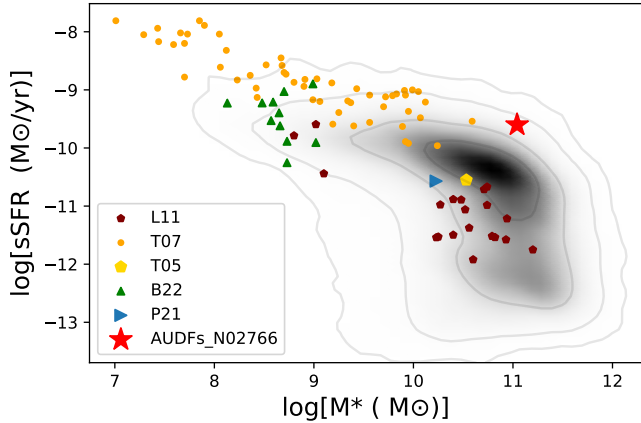


Figure 4. A comparison of sSFR vs stellar mass of AUDFs_N02766 and all the detected XUV disks (L11:Lemonias et al. (2011), T07:Thilker et al. (2007), T05: Thilker et al. (2005), B22:Borghain et al. (2022), P21:Padave et al. (2021)) along with the population of galaxies at $z \approx 0$ shown in Black Salim et al. (2016).

7.2 Star formation in XUV region and central quenching

Comparison of the N242W observations with archival optical and infrared data reveals that star formation in AUDFs_N02766 is spatially extended across the stellar disk. The dust-corrected, intrinsic rest-frame FUV SB profile shows that the SFR threshold lies well beyond the optical radius, whereas the older stellar population is concentrated near the central bulge. This central buildup may result from the cold gas accretion in the outer parts, forming clumps and their subsequent inward migration, potentially driving morphological transformation toward an early-type system (Elmegreen et al. 2008; Dekel et al. 2009b; Saha & Cortesi 2018; Borghain et al. 2022). From our best-fit rest-frame FUV model, we estimate the total SFR in the XUV region ($4.5'' < r < 9''$) to be $\sim 2.8 M_{\odot} \text{ yr}^{-1}$. Since the reported star formation efficiency of outer disk regions of galaxies, in general, is very low, the gas reserves would not be depleted by the ongoing star formation within a Hubble timescale (Bigiel et al. 2010; Borghain et al. 2022). The inferred gas accretion rate from the intergalactic medium is $\sim 11 M_{\odot} \text{ yr}^{-1}$ indicating a gas replenishment rate that exceeds ongoing star formation and is capable of sustaining the observed growth in the outer disk for a very long time.

Within the inner disk ($r < 4.5''$), the intrinsic rest-frame FUV model-derived SFR is relatively high at $\sim 25 M_{\odot} \text{ yr}^{-1}$, despite the central rest-frame FUV surface brightness profile being notably flat. This may indicate the onset of central quenching (Tacchella et al. 2015), consistent with the formation of a passive bulge and declining star formation in the core. The presence of an active galactic nucleus (AGN) remains a possibility, potentially contributing to gas removal or heating through feedback, thereby suppressing star formation in the central region (Fabian 2012).

7.3 A comparison with other XUV studies

In Figure 4, the specific star formation rate (sSFR) of AUDFs_N02766 is noticeably higher than that of the local star-forming galaxy population. A general anti-correlation is observed in the $\log(\text{sSFR})$ versus $\log(\text{stellar mass})$ plane for all detected XUV disks, relative to the average galaxy population.

AUDFs_N02766, however, stands out with a significantly higher sSFR compared to locally identified massive XUV systems ($z \sim 0$). This enhancement may reflect the general increase in gas fraction with redshift (Kanekar et al. 2016), which provides more fuel for star formation in the outer disk. Furthermore, the different environments and composition of galaxies at higher redshifts could play a critical role in shaping the properties and extent of XUV emission.

The anti-correlation in Figure 4 could be driven by the shallow potential wells of low-mass galaxies, where gas can be more diffusely distributed, enabling more extended star formation. Additionally, most photometric surveys rely on optical bands for source detection, which can miss faint, extended UV features in such galaxies. As a result, lower-mass XUV galaxies might be deriving a larger fraction of their total star formation from the XUV region. We may currently be missing such XUV disk galaxies at intermediate redshifts, which could be promising targets for future wide-field surveys such as the Vera C. Rubin Observatory (LSST; Ivezić et al. (2019)), as well as upcoming UV missions (e.g. CASTOR; Cote et al. (2019)).

8 CONCLUSIONS

We summarize the key findings of this study below:

- We report the detection of a very massive and strongly star-forming extended ultraviolet (XUV) disk galaxy, AUDFs_N02766, at a redshift of $z \approx 0.67$. The XUV emission extends to nearly twice the optical size of the galaxy.
- This represents the most distant XUV disk galaxy identified to date.
- AUDFs_N02766 exhibits a well-defined central bulge composed of older stellar populations, accompanied by widespread star formation across the disk and clumpy, UV-bright features in the outer regions. These characteristics support its classification as a mixed-type XUV disk (Types I + II).
- From its measured lopsidedness, we estimate an average gas accretion rate of $\sim 11 M_{\odot} \text{ yr}^{-1}$, that appears sufficient to sustain the ongoing star formation in the XUV disk.

ACKNOWLEDGEMENTS

We thank the anonymous referee for their constructive feedback, which improved this manuscript. P.P. acknowledges Anshuman Borghain, Soumil Maulick, Suraj Dhiwar, and the AUDF group for valuable discussions and input on the methodology.

DATA AVAILABILITY

The UVIT data used in this study are not yet publicly available, but can be provided upon reasonable request to the corresponding author. All other datasets used in this work are publicly available from archival sources.

REFERENCES

- Astropy Collaboration et al., 2022, *ApJ*, **935**, 167
 Balestra I., et al., 2010, *A&A*, **512**, A12
 Bigiel F., Leroy A., Walter F., Blitz L., Brinks E., de Blok W. J. G., Madore B., 2010, *AJ*, **140**, 1194
 Boquien M., 2020, in American Astronomical Society Meeting Abstracts #235. p. 228.01

Borghain A., Saha K., Elmegreen B., Gogoi R., Combes F., Tandon S. N., 2022, *Nature*, **607**, 459

Bradley L., et al., 2024, *astropy/photutils*: 1.12.0, doi:10.5281/zenodo.596036

Bruzual G., Charlot S., 2003, *MNRAS*, **344**, 1000

Calzetti D., Armus L., Bohlin R. C., Kinney A. L., Koornneef J., Storchi-Bergmann T., 2000, *ApJ*, **533**, 682

Cote P., et al., 2019, in Canadian Long Range Plan for Astronomy and Astrophysics White Papers. p. 18, doi:10.5281/zenodo.3758463

Das M., Yadav J., Patra N., Dwarakanath K. S., McGaugh S. S., Schombert J., Rahna P. T., Murthy J., 2021, *Journal of Astrophysics and Astronomy*, **42**, 85

Dekel A., Birnboim Y., 2006, *MNRAS*, **368**, 2

Dekel A., et al., 2009a, *Nature*, **457**, 451

Dekel A., Sari R., Ceverino D., 2009b, *ApJ*, **703**, 785

Dhiwar S., Saha K., Dekel A., Paswan A., Pandey D., Cortesi A., Pandge M., 2023, *MNRAS*, **518**, 4943

Draine B. T., et al., 2014, *ApJ*, **780**, 172

Elmegreen B. G., Bournaud F., Elmegreen D. M., 2008, *ApJ*, **688**, 67

Fabian A. C., 2012, *ARA&A*, **50**, 455

Gil de Paz A., et al., 2005, *ApJ*, **627**, L29

Gil de Paz A., et al., 2007a, *ApJS*, **173**, 185

Gil de Paz A., et al., 2007b, *ApJ*, **661**, 115

Goddard Q. E., Kennicutt R. C., Ryan-Weber E. V., 2010, *MNRAS*, **405**, 2791

Goddard Q. E., Bresolin F., Kennicutt R. C., Ryan-Weber E. V., Rosales-Ortega F. F., 2011, *MNRAS*, **412**, 1246

Hogg D. W., Baldry I. K., Blanton M. R., Eisenstein D. J., 2002, *arXiv e-prints*, pp astro-ph/0210394

Hopkins P. F., Hernquist L., Cox T. J., Kereš D., 2008, *ApJS*, **175**, 356

Illingworth G., et al., 2016, *arXiv e-prints*, p. arXiv:1606.00841

Inoue A. K., 2011, *MNRAS*, **415**, 2920

Inoue A. K., Iwata I., Deharveng J.-M., 2006, *MNRAS*, **371**, L1

Ivezić Ž., et al., 2019, *ApJ*, **873**, 111

Jog C. J., Combes F., 2009, *Phys. Rep.*, **471**, 75

Kanekar N., Sethi S., Dwarakanath K. S., 2016, *ApJ*, **818**, L28

Kennicutt Robert C. J., 1998, *ARA&A*, **36**, 189

Kennicutt R. C., Evans N. J., 2012, *ARA&A*, **50**, 531

Lemonias J. J., et al., 2011, *ApJ*, **733**, 74

López-Sánchez Á. R., Westmeier T., Esteban C., Koribalski B. S., 2015, *MNRAS*, **450**, 3381

Moffett A. J., Kannappan S. J., Baker A. J., Laine S., 2012, *ApJ*, **745**, 34

Momcheva I. G., et al., 2016, *ApJS*, **225**, 27

Muñoz-Mateos J. C., Gil de Paz A., Boissier S., Zamorano J., Jarrett T., Gallego J., Madore B. F., 2007, *ApJ*, **658**, 1006

Neff S. G., et al., 2005, *ApJ*, **619**, L91

Padave M., et al., 2021, *ApJ*, **923**, 199

Padave M., et al., 2024, *ApJ*, **960**, 24

Pandey P., Saha K., 2025, *ApJS*, **276**, 52

Peng C. Y., Ho L. C., Impey C. D., Rix H.-W., 2010, *AJ*, **139**, 2097

Pohlen M., Trujillo I., 2006, *A&A*, **454**, 759

Retzlaff J., Rosati P., Dickinson M., Vandame B., Rité C., Nonino M., Cesarsky C., GOODS Team 2010, *A&A*, **511**, A50

Rix H.-W., Zaritsky D., 1995, *ApJ*, **447**, 82

Saha K., Cortesi A., 2018, *ApJ*, **862**, L12

Saha K., Jog C. J., 2014, *MNRAS*, **444**, 352

Saha K., et al., 2020, *Nature Astronomy*, **4**, 1185

Saha K., et al., 2024, *ApJS*, **275**, 28

Salim S., et al., 2016, *ApJS*, **227**, 2

Sarkar S., Saha K., 2024, *arXiv e-prints*, p. arXiv:2409.20309

Schlafly E. F., Finkbeiner D. P., 2011, *ApJ*, **737**, 103

Schlegel D. J., Finkbeiner D. P., Davis M., 1998, *ApJ*, **500**, 525

Skelton R. E., et al., 2014, *ApJS*, **214**, 24

Somerville R. S., Davé R., 2015, *ARA&A*, **53**, 51

Stefanon M., et al., 2021, *ApJS*, **257**, 68

Tacchella S., et al., 2015, *Science*, **348**, 314

Thilker D. A., et al., 2005, *ApJ*, **619**, L79

Thilker D. A., et al., 2007, *ApJS*, **173**, 538

Tolman R. C., 1930, *Proceedings of the National Academy of Science*, **16**, 511

Tolman R. C., 1934, *Relativity, Thermodynamics, and Cosmology*

Virtanen P., et al., 2020, *Nature Methods*, **17**, 261

Whitaker K. E., et al., 2019, *ApJS*, **244**, 16

Windhorst R. A., et al., 2011, *ApJS*, **193**, 27

Zaritsky D., Christlein D., 2007, *AJ*, **134**, 135

Zaritsky D., Rix H.-W., 1997, *ApJ*, **477**, 118

APPENDIX A: SPECTRUM AND OBSERVATIONS

The released spectrum of AUDFs_N02766 from VLT-Vimos survey by (Balestra et al. 2010) is shown in figure A1 along with highlighted features, which were prominent and helped in redshift determination.

All the broadband observations of AUDFs_N02766 from AstroSat-UVIT, Spitzer-IRAC, VLT-ISAAC, and HST shown in figure A2.

APPENDIX B: PSF MATCHING

The PSF matching routine for HST and ISAAC images to the N242W is listed below.

- We identified isolated stars in the N242W image and ISAAC bands to model their PSF with a central moffat and extended exponential component, whose 1D radial profiles are shown in figure B1.
- Obtained the HST-F160W psf provided from Momcheva et al. (2016).
- Psf matching kernels were obtained with photutils psf matching routine, after scaling all psfs to the same pixel scale.
- The PSF matching kernels were tested by convolving HST psf and ISAAC psfs models, and comparing their curve of growth profiles with the curve of growth profile of NUV PSF (figure B1).

We briefly discussed the depth differences between UVIT N242W and HST-UV bands (F225W, F275W) in the main text; here, we directly compare their surface brightness (SB) profiles in Figure B1d, with HST data PSF-matched to N242W. While the HST-UV profiles generally follow the N242W shape, their large uncertainties at low SB levels make them unsuitable for tracing the extended XUV disk, unlike the deeper and higher S/N N242W data.

APPENDIX C: PHOTOMETRY AND SED FITTING

We work on Image cutouts of size $\sim 32.1'' \times 32.1''$ obtained around the galaxy coordinates in the UVIT- F154W and N242W bands (77×77 pixels) and deep archival Optical and IR data, which are Issac- J, H, Ks bands (215×215 pixels), Irac- 1,2,3,4 bands (107×107 pixels) and HST(convolved to F160W psf)- F336W, F435W, F606W, F775W, F814W, F850LP, F098M, F125W, F140W, F160W bands (539×539 pixels). All cutouts are shown in Appendix A.

To estimate the local background in UVIT data, 10 semi-random 5×5 pixel boxes were placed away from HST optical and UV sources. For the N242W cutout, the local mean and sigma were 1.2×10^{-4} and 4.2×10^{-5} cps/pixel, yielding a 3σ depth of 28.56 mag/arcsec². Given the crowded GOODS-South region, we also used a minima-based background estimator (Pandey & Saha 2025) over a larger $70''$ cutout, which returned consistent values: 1.17×10^{-4} cps/pixel (mean) and 4.24×10^{-5} cps/pixel (sigma). For FUV154W, the background mean and sigma were 4.3×10^{-6} and 8.3×10^{-5} cps/pixel, respectively.

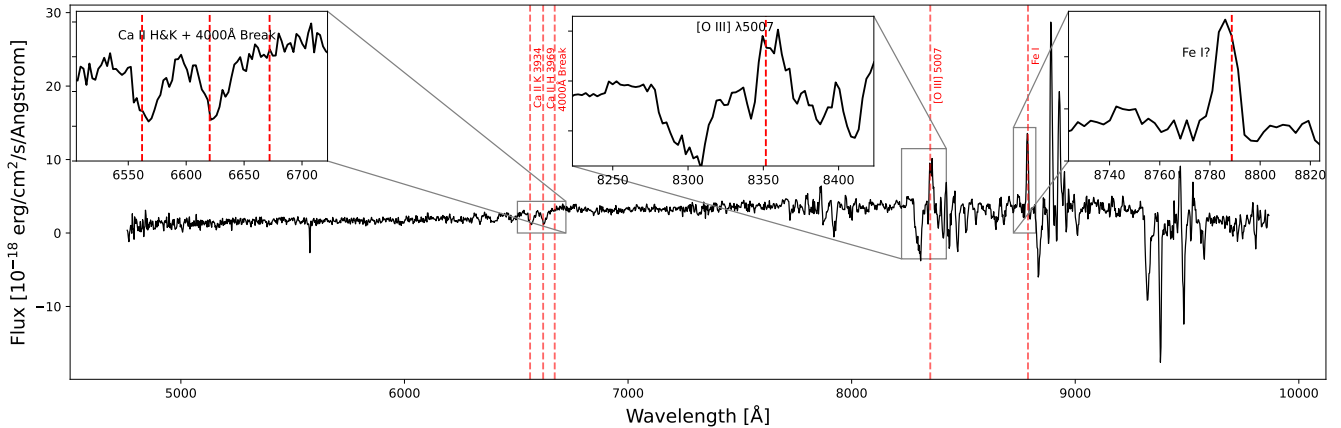


Figure A1. The optical spectrum of AUDFs_N02766 as observed by the VLT-Vimos survey (Balestra et al. 2010)

To ensure consistent flux measurements across bands, we PSF-matched the HST and ISAAC images to the UVIT N242W resolution. This was done using the PSF matching routine from Photutils (Bradley et al. 2024), with full details provided in Appendix B. The F154W band has a curve of growth (COG) that closely matches that of N242W beyond $r > 2''$, with deviations under 1% (Saha et al. 2024), and thus was not further adjusted. The IRAC bands, particularly IRAC-2, 3, and 4, have significantly broader PSFs than UVIT. PSF matching to IRAC resolution would risk contamination from nearby sources; therefore, we used aperture-corrected fluxes directly from the observed images for these bands.

We define a visually selected circular aperture with a radius of $4.58''$ centered on the galaxy’s bulge, encompassing nearly all flux within the optical extent and avoiding contamination from nearby sources. This aperture is applied uniformly across all bands (F154W, N242W, PSF-matched HST and ISAAC images, and IRAC bands). Fluxes and associated uncertainties are measured using the corresponding weight maps, which are PSF-convolved for the HST and ISAAC images. For UVIT bands, flux uncertainties are computed as the Poissonian standard deviation of the total flux and background within the aperture, given by:

$$\Delta f = \frac{\sqrt{(f + b \times A) \times t_{\text{exposure}}}}{t_{\text{exposure}}}, \quad (\text{C1})$$

where f is the calculated flux of the galaxy within the aperture, b is the mean background per pixel, A is the aperture area in pixels and t_{exposure} is the total exposure time of the image.

Aperture correction factors were calculated for the used aperture from the PSF of all bands and multiplied by the aperture flux and aperture flux errors of the galaxy. The observed magnitudes are presented in the Table C1.

To construct the broadband spectral energy distribution (SED) of the galaxy from the far-UV to the infrared (1300 \AA to $9.5 \mu\text{m}$), we use the SED fitting code CIGALE (Boquien 2020). Observed fluxes were first converted to milliJansky and corrected for foreground extinction at the effective wavelength of each filter.

The following CIGALE modules were used:

- `sfh2exp`: double exponential star formation history,
- `bc03`: (Bruzual & Charlot 2003) single stellar population models,
- `nebular`: (Inoue 2011) nebular continuum and line emission,

- `dustatt_modified_starburst`: modified Calzetti (2000) (Calzetti et al. 2000) attenuation law,
- `d12014`: (Draine et al. 2014) dust emission model.

We explored various dust attenuation laws corresponding to the Milky Way (MW), Large Magellanic Cloud (LMC), and Small Magellanic Cloud (SMC). While all yielded similar star formation histories, the best-fitting model (reduced $\chi^2 = 1.2$) was obtained using Milky Way attenuation parameters. The resulting SED fit yields a stellar mass of $1.083 \times 10^{11} M_{\odot}$, a young stellar component of $2.64 \times 10^8 M_{\odot}$, and a star formation rate (SFR) of $28.1 \pm 1.4 M_{\odot} \text{ yr}^{-1}$. The best-fit color excess is $E(B - V) = 0.132$.

APPENDIX D: ROBUSTNESS OF CLUMP DETECTION AND MEASUREMENT

To detect clumps in the XUV region as individual sources, we adopt the hot-mode detection strategy outlined in Saha et al. (2024), applied to the N242W band. However, we modify two key SExtractor parameters: `DETECT_MINAREA` and `DEBLEND_MINCONT`, to 5 pixels and 5×10^{-6} respectively. This adjustment is motivated by our goal of identifying extremely faint sources constituting the clumpy XUV disk. Since the clumps are expected to be compact and barely resolved, we set `DETECT_MINAREA` close to the area subtended by the N242W PSF FWHM, which covers $\sim 5-6$ pixels. This maximises our sensitivity to faint point-like sources. Additionally, a lower `DEBLEND_MINCONT` value is used to better separate overlapping clumps based on pixel contrast. All other parameters follow the standard hot-mode configuration in Saha et al. (2024).

All optical HST sources within the XUV region appear point-like at the resolution of the N242W band. To verify the independence of the detected clumps, we search for optical counterparts within a $1.2''$ aperture—the FWHM of the N242W PSF. Detections with clear HST counterparts at different redshifts are excluded from further consideration. Also, for the overlapping clumps (within a PSF FWHM radius aperture), we remove the less significant detection. The remaining clumps without corresponding optical sources are listed in Table 1 of main text.

Clump C6 has an optical counterpart with $z_{\text{phot}} = 0.65$, visible across all bands; it could be a satellite of AUDFs_N02766 with an older stellar population, or a foreground/background galaxy. The elliptical feature E1 coincides with a source at $z_{\text{phot}} = 4.2$, which

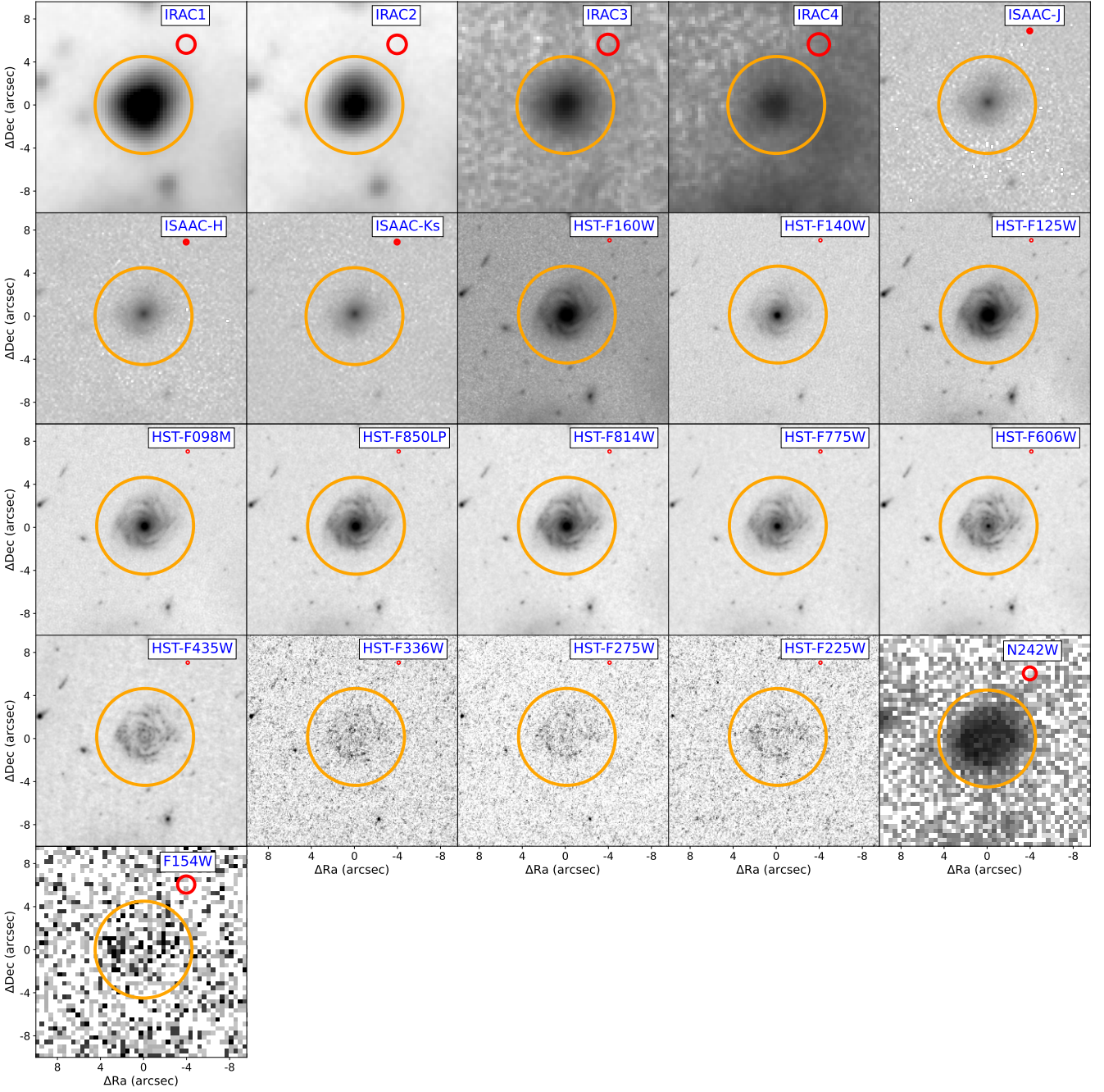


Figure A2. Multi-band observations of ADFs_N02766 from UVIT, HST (WFC3-ACS), ISAAC, and IRAC. Filter names and their PSF-FWHM are indicated at the top right of each panel. Red circles denote PSF-FWHM: HST ($0.095''\text{--}0.2''$), ISAAC ($0.3''\text{--}0.5''$), IRAC ($1.6''\text{--}2.0''$), and UVIT (N242W: $1.2''$, F154W: $1.6''$). The orange circle represents the circular aperture used for the photometry of ADFs_N02766 in these bands.

would place the red edge of the N242W filter below the Lyman limit ($\lambda < 912 \text{ \AA}$) for this object. Given the rarity of confirmed LyC emitters, we interpret E1 as a morphological feature of ADFs_N02766.

To assess the reliability of the detected clumps and rule out spurious noise peaks, we perform two tests using a $3' \times 3'$ test patch from the GOODS-South field in the N242W filter, located $\sim 5'$ south of the centre of ADFs_N02766, where background conditions are similar. We run SExtractor with the same parameters as used for clump detection and perform aperture photometry using $1.2''$ radius aper-

tures. The AB magnitude (calculated within a $1.2''$ radius aperture) distribution of sources is shown as a grey histogram in Figure D1b,c, with a 3σ detection threshold marked.

To assess false detections, we masked the N242W patch using the HST segmentation map (resampled to the N242W scale), masking an additional $2''$ wide region around each segmentation to account for the broader PSF ($\text{FWHM} = 1.2''$). We then placed 50 non-overlapping circular apertures with radii equal to the PSF FWHM in the unmasked regions and measured the aperture SNR and mag-

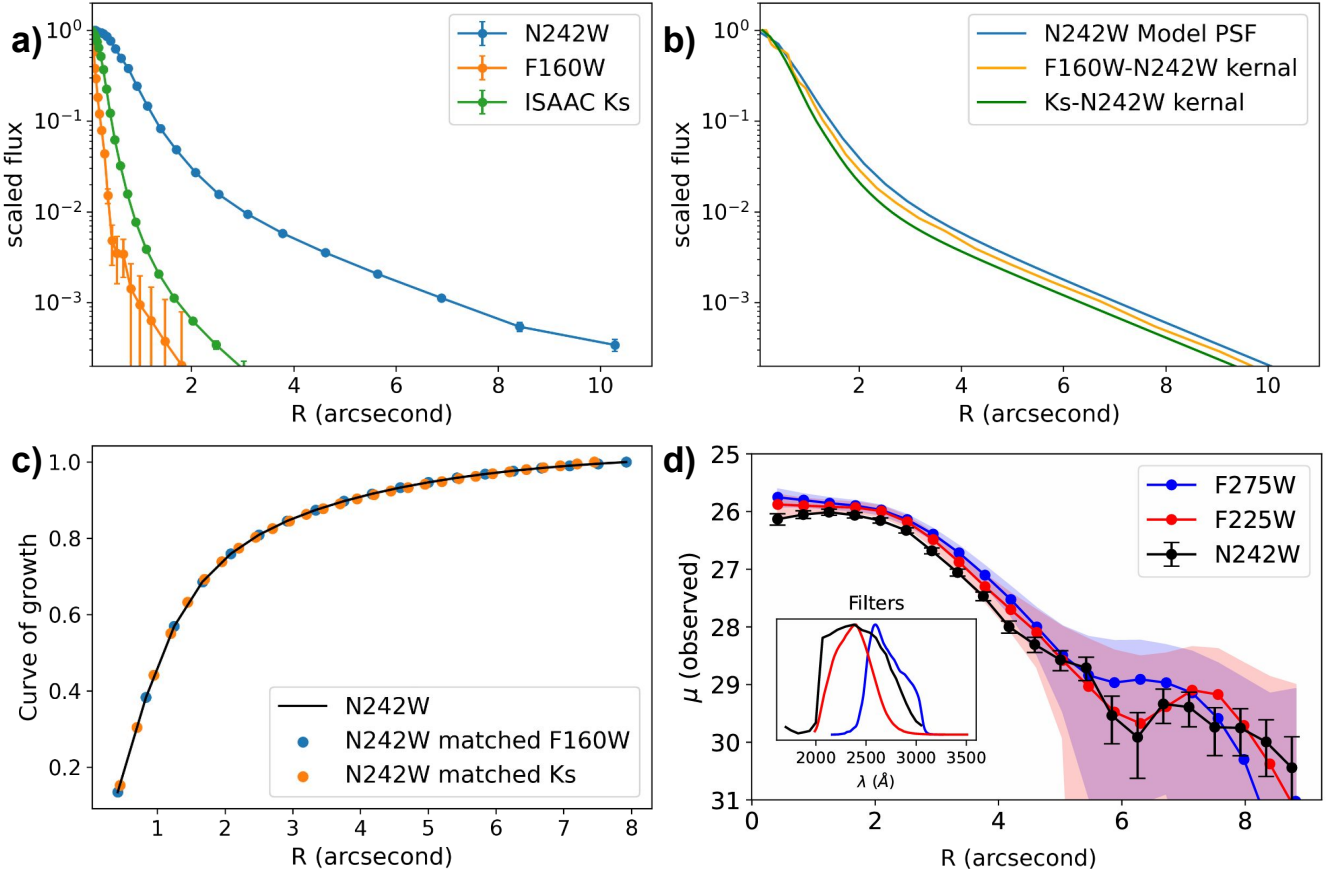


Figure B1. (a) 1-D profile of star stacks of UVIT-N242W (blue-cyan), HST-F160W (orange), and ISAAC-Ks bands (green), with their peak values scaled to one for comparison. (b) The NUV model PSF (blue-cyan) with PSF matching kernels obtained for matching F160W (yellow) and ISAAC-Ks with N242W (green) (c) The curve of growth profiles of N242W, N242W psf matched F160W and ISAAC-Ks bands. (d) Surface brightness (SB) profiles of AUDFs_N02766 in the HST-UV bands (F225W and F275W), PSF-matched to the N242W resolution, compared with the N242W SB profile. Shaded regions indicate uncertainties in the HST-UV profiles. All profiles are shown without correction for extinction or attenuation.

Telescopes	Filters and Integrated Magnitudes (Observed)			
UVIT	N242W	F154W		
	22.19 ± 0.02	23.62 ± 0.08		
HST	F160W	F140W	F125W	F098W
	19.09 ± 0.002	19.25 ± 0.006	19.34 ± 0.002	19.65 ± 0.003
	F850LP	F814W	F775W	F606W
	19.82 ± 0.003	20.03 ± 0.003	20.12 ± 0.004	20.98 ± 0.005
	F435W	F336W	F275W	F225W
	21.94 ± 0.008	21.67 ± 0.04	22.12 ± 0.04	22.03 ± 0.04
SPITZER	IRAC-1	IRAC-2	IRAC-3	IRAC-4
	18.80 ± 0.001	19.21 ± 0.002	19.20 ± 0.003	19.34 ± 0.004
VLT-ISAAC	H	J	Ks	
	19.62 ± 0.02	19.28 ± 0.01	18.98 ± 0.02	

Table C1. Photometry of AUDFs_N02766 across all the bands shown in Figure A2.

nitudes. The results are shown as coloured histograms in Fig. D1b (excluding the blue histogram), alongside all SExtractor detections in the patch (grey). Repeating this test five times yielded 250 aperture samples, of which only six exceeded the 3σ detection threshold, corresponding to a false detection rate of 0.024 per aperture. Given that the XUV region spans $\sim 151 \text{ arcsec}^2$ (accommodating ~ 33 apertures), the expected number of false positives is ~ 0.8 . In comparison, we detect six clumps above the detection limit, a number

that significantly exceeds the expectation from noise. For clump detection around AUDFs_N02766, we did not apply the extra $2''$ buffer to its optical segmentation in order to maximise recovery of isolated star-forming complexes in the XUV region. Even when this buffer is applied, clumps C1, C2, C3 and C4 remain detectable, as they lie at projected radii $r > 6.5''$, i.e. at least $2''$ beyond the galaxy's optical radius of $4.5''$.

In our second test, we show the robustness of our source extractor

parameters. Here, we quantify the spurious detections that populate the high-magnitude end ($mag > 3\sigma$ detection limit) of the detections in the test patch (grey histogram in Figures D1b and c). We simulate five Poisson random patches of the same size as the test patch, with the same noise properties of our N242W image, and no sources. We run SExtractor with the same parameters on these simulated patches and calculate the number of spurious detections. The colored histograms (not blue) in figure D1 c, show that the population of these spurious detections peak at ~ 29 magnitudes, and falls sharply towards the 3σ detection limit ($mag_{3\sigma} = 27.73$). Also, we see that in almost all five iterations of this test, we get that the number of false detections in the simulated patch \geq number of detections in the N242W patch for magnitudes > 29 . Thus, we interpret that all the detections in the grey histogram (Figure D1) with > 29 magnitudes are likely spurious detections. And a significant portion of the detected sources between 27.73 & 29 magnitudes might be spurious too. We performed this test to determine whether the detected clumps were spurious in nature. Across five simulated patches, only two false detections were found with magnitudes brighter than 27.73. The results correspond to a false-positive rate of ~ 0.044 sources per arcmin², which, when scaled to the XUV region (~ 151 arcsec² or ~ 0.042 arcmin²), yields an expected false detection rate of just ~ 0.0018 sources brighter than the 3σ detection limit, making it extremely unlikely that even one of the detected clumps are such false positives.

APPENDIX E: INNER DISK'S CONTRIBUTION TO THE XUV REGION IN N242W

As discussed in the main text, the XUV region is affected by flux boosting from the inner bright disk due to the N242W PSF (Fig. Ba). While this is accounted for via forward modelling of the full disk, it is also important to demonstrate that the extended emission seen in N242W is not entirely produced by the inner disk and requires an additional component. To test this, we compare the N242W observation of AUDFs_N02766 with the UV inner-disk model derived from HST/F225W, convolved with the N242W PSF.

The HST UV images (Fig. A2) show a ring-like pattern in the inner disk. This appearance is caused by star-forming clumps located along the tightly wound spiral arms (Fig. E1). The same structure produces a bump in the HST/F225W surface-brightness profile (Fig. E2), which we model using a Gaussian ring (Eq. E1) together with a Sérsic component for the inner disk. The resulting 2D model, along with the F225W image and residuals, is shown in Fig. E3.

$$r_{ell}(x, y) = \sqrt{(x)^2 + \left(\frac{y}{1 + \epsilon}\right)^2}$$

$$\implies I(r_{ell}) = I_0 \exp\left[-\left(\frac{r_0 - r_{ell}}{2\sigma}\right)^2\right] \quad (\text{E1})$$

The model is convolved with the N242W PSF, and its surface-brightness profile is compared with the observed N242W profile in Fig. E4.

An excess of UV flux is evident in the N242W surface-brightness profile compared to the PSF-convolved model in the XUV region (Fig. E4). Beyond $r > 9''$, the N242W profile becomes noisy, as the measurements are affected by heavy masking of foreground and background UV sources. Owing to these uncertainties, we restrict the XUV measurement to $r < 9''$.

We also compare the integrated magnitude of the XUV region between the PSF-convolved HST/F225W model and the N242W data, where we find that

$$\Delta m_{xuv} = m_{xuv, N242W} - m_{xuv, F225W*} = -0.57 \pm 0.067 \quad (\text{E2})$$

Here, $m_{xuv, N242W}$ denotes the integrated magnitude of the XUV region ($4.5'' < r < 9''$) in the N242W band, and $m_{xuv, F225W*}$ the integrated magnitude of the same region in the PSF-matched HST/F225W band. Both magnitudes were measured after applying the point-source masking described in the main text.

The resulting $\Delta m_{xuv} = -0.57 \pm 0.067$ implies that the N242W XUV region is 1.7 ± 0.1 times brighter than expected from the PSF-convolved F225W inner-disk model. Thus, 41 ± 4 per cent of the total emission in the N242W XUV region ($4.5'' < r < 9''$) originates from the extended UV disk rather than the inner disk.

APPENDIX F: SURFACE BRIGHTNESS CORRECTIONS

To obtain the rest-frame FUV and K_s -band surface brightness (SB) profiles, we apply cosmological surface brightness dimming, internal dust correction, and Galactic foreground extinction.

The cosmological dimming correction follows the relation from Hogg et al. (2002):

$$f_\nu(\nu_o) = \frac{L_\nu(\nu_e)(1+z)}{4\pi D_L^2}, \implies \mu(\nu_e) = \mu(\nu_o) - 2.5 \log(1+z)^3, \quad (\text{F1})$$

where D_L and D_A are the luminosity and angular diameter distances ($D_L = D_A(1+z)^2$), L_ν and f_ν are the luminosity and flux densities, ν_e and ν_o are emitted and observed frequencies, and μ is the SB in mag arcsec⁻², given by $\mu = ZP - 2.5 \log(f/a)$, with ZP the filter zeropoint and a the aperture area in arcsec².

For our galaxy at $z = 0.67$, the cosmological correction factor is $A_{\text{cosmo}} = -2.5 \log(1.67)^3 = -1.670$.

The internal dust correction is derived from the best-fit SED, giving $E(B - V)$ consistent with $A_{\text{dust}} = -1.227$ at the rest-frame FUV wavelength ($\lambda = 242/1.67 = 145$ nm) using the Calzetti et al. (2000) dust attenuation law. This correction is negligible in the K_s band.

Foreground Galactic extinction values are taken from the NED extinction calculator, yielding $A_{\text{fore}} = -0.054$ for N242W (negligible for IRAC-1).

The total correction for the rest-frame FUV SB profile is thus:

$$\mu_{FUV}(\lambda_e = 145 \text{ nm}) = \mu(\lambda_o = 242 \text{ nm}) + A_{\text{cosmo}} + A_{\text{dust}} + A_{\text{fore}} \quad (\text{F2})$$

$$= \mu(\lambda_o = 242 \text{ nm}) - 2.951. \quad (\text{F3})$$

For the rest-frame K_s band ($\lambda_e = 2.2 \mu\text{m}$) derived from IRAC-1 ($\lambda_o = 3.6 \mu\text{m}$), only the cosmological correction is significant:

$$\mu_{K_s}(\lambda_e = 2.2 \mu\text{m}) = \mu(\lambda_o = 3.6 \mu\text{m}) - 1.670. \quad (\text{F4})$$

Thus, the N242W SB profile requires a total correction of ≈ 3 magnitudes to obtain the rest-frame FUV SB profile, and the IRAC-1 SB profile requires ≈ 1.67 magnitudes correction to obtain the rest frame K_s profile.

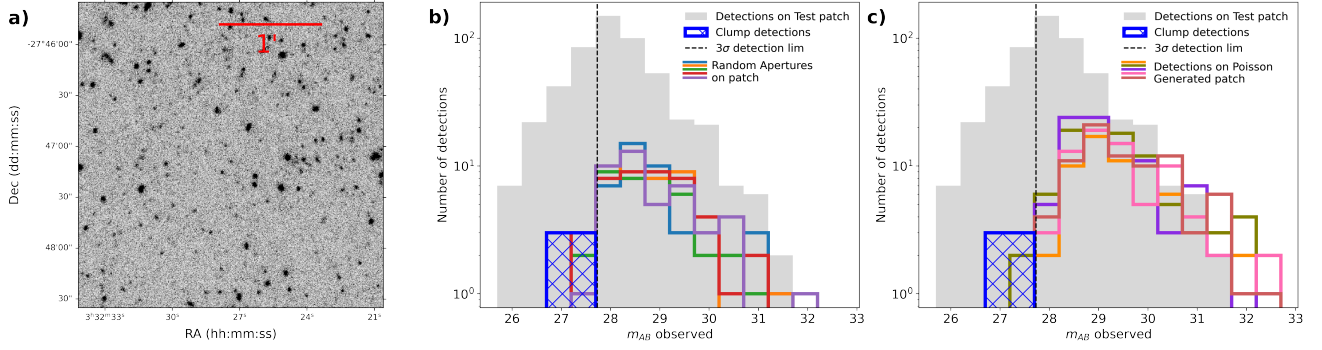


Figure D1. (a) A $3' \times 3'$ test patch from the N242W observations in the AUDF-Goods South field, located near AUDFs_N02766 (b) AB magnitude distribution of sources detected in the test patch: the blue-hatched histogram represents the UV clumps detected in the XUV region (see Figure 1b and Table 1), overlaid on a gray histogram of all sources in the patch. Colored histograms show fluxes from 250 randomly placed apertures ($r = 1.2''$) to evaluate the likelihood of false detections. The dashed black line marks the 3σ detection threshold. (c) Same as (b), but here the colored histograms represent detections from empty, noise-only simulated patches created with Poisson noise matched to the background of the test patch.

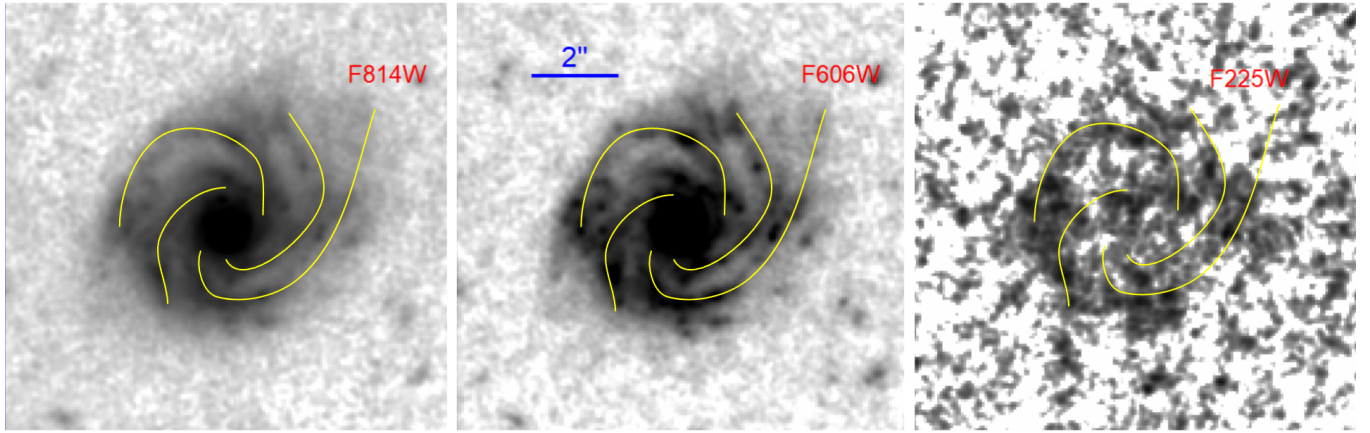


Figure E1. Cutouts of AUDFs_N20766 in HST-F814W (left), F606W (middle) and F225W (right), where we have marked the visible spiral arms in F814W (rest frame- 487 nm) and F606W (rest frame- 362 nm) with yellow curves. (right) Over-plotted spiral arm markers on smoothed F225W observation (rest frame- 134 nm), showing the orientation of star-forming complexes with respect to the spiral arms.

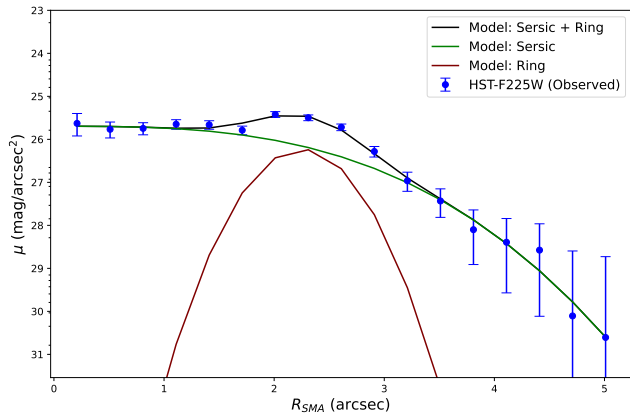


Figure E2. Observed surface Brightness profile of AUDFs_N20766 in F225W in the inner disk, fitted with a Sersic + Gaussian Ring model.

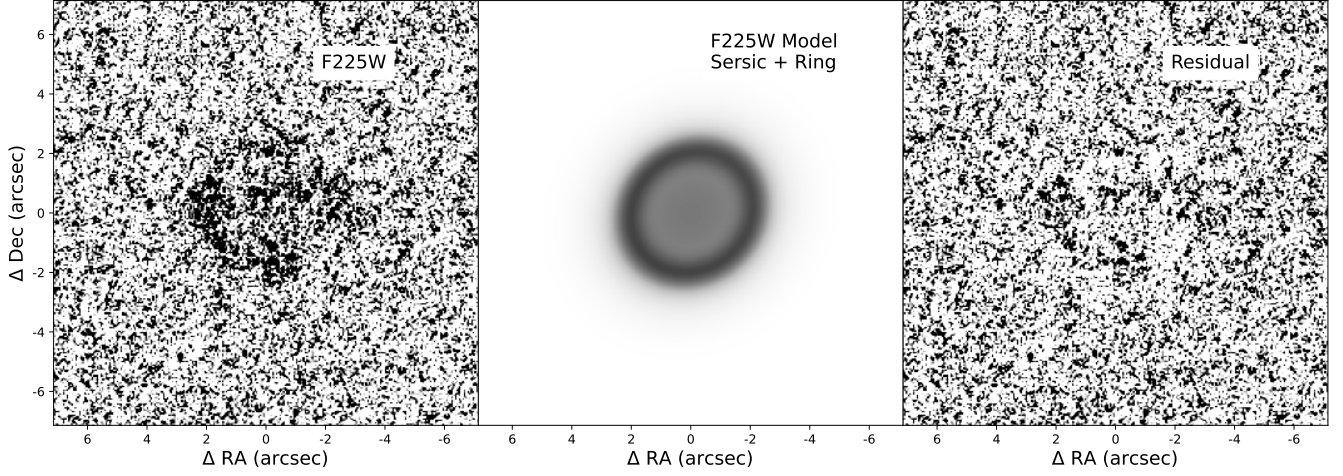


Figure E3. (left) F225W cutout of AUDFs_N20766. (middle) 2D model of the inner disk modelled in Figure E2. (right) residual after subtraction of the 2D model deconvolved F225W.

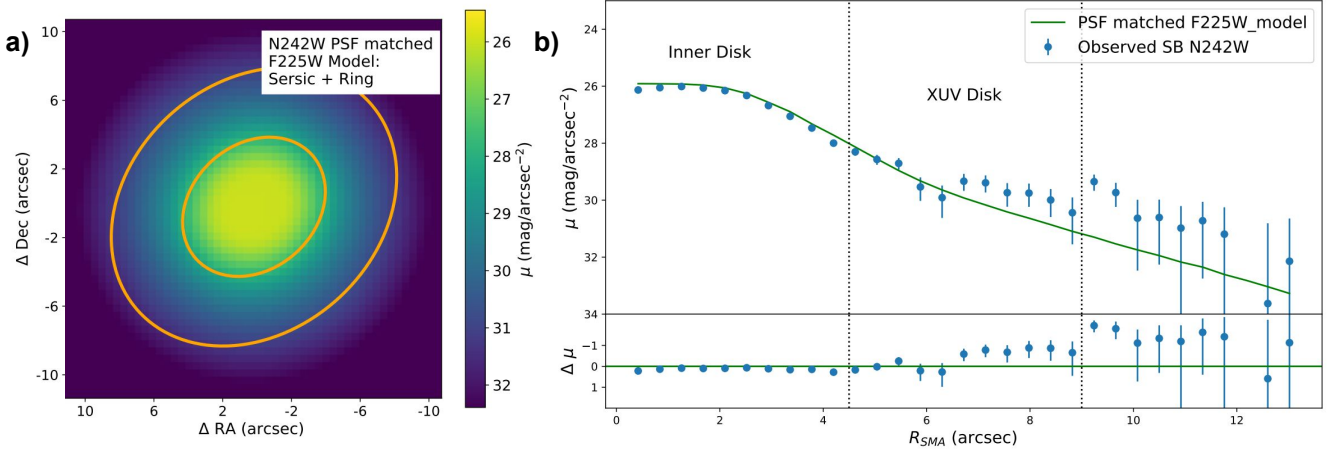


Figure E4. (a) 2D model of the inner disk in F225W, convolved with the UVIT-N242W PSF, along with the elliptical annulus marking the region between $4.5'' < r_{SMA} < 9''$, where we observe the XUV emission in N242W. (b) The Observed surface brightness profile of AUDFs_N20766 in N242W band, along with the surface brightness profile of the UVIT PSF convolved model of the inner disk, where the difference between the SB profiles of N242W and PSF convolved F225W model is also shown.